Clustering-Based Automated Generation and Multiscale Analysis of Metamaterial Representative Volume Elements

Nima Dolatabadi[1], Renato Zona[2], Maziar Zahed[1(✉)], and Vincenzo Minutolo[2]

[1] Dipartimento di Ingegneria Civile-Industriale e Architettura, Università di Catania, Via Santa Sofia 64, 95123 Catania, Italy
maziar.zahed@phd.unict.it

[2] Dipartimento di Ingegneria, Università degli Studi della Campania Luigi Vanvitelli, Via Roma 29, 81031 Aversa, CE, Italy
renato.zona@unicampania.it

Abstract. Drawing on representative volume elements (RVEs), artificial intelligence (AI) approaches and computational methods, an automated methodology was integrated to generate and assess mechanical metamaterials. The method is aimed at directly converting image-based inputs into 3D geometries independently of manual CAD simulations to substantially accelerate preprocessing.

This study performed material region identification and complex geometry reconstruction through learning-based image segmentation and incorporated filtering into the method to establish a feasible structure and discard configurations with mechanical inconsistency and/or instability.

Emphasizing the dependence of key mechanical properties on geometric variables, lattice-based structures were evaluated to validate the proposed method. The equivalent modulus of elasticity was found to be smaller relative to the base material by up to two orders of magnitude, with the numerical results being in good agreement with experimental data. The computational cost was also found to be remarkably (≈95%) lower than conventional modeling.

This effective and efficient methodology with superb scalability can be employed in a range of applications, including additive manufacturing (AM), multiscale modeling, and structural engineering, where metamaterials are designed and analyzed in an automated manner.

Keywords: Metamaterials · Representative Volume Element · Image Segmentation · Artificial Intelligence · Homogenization · Finite Element Analysis

1 Introduction

To develop architected metamaterials, it is vital to carefully evaluate their mechanical behavior, as predicting elastic and plastic responses under vari-

© The Author(s), under exclusive license to Springer Nature Switzerland AG 2027
O. Gervasi et al. (Eds.): ICCSA 2026 Workshops, LNCS 16762, pp. 583–598, 2027.
https://doi.org/10.1007/978-3-032-30524-4_36

ous loads is essential for engineering applications. However, the microstructural topology quite effects the prediction of homogenized elastic responses in lattice designs, particularly under stochastic and periodic loads. To address this challenge, researchers have developed inverse design approaches aimed at achieving specific stress-strain profiles or mechanical constants. For instance, Cao et al. [1] introduced a deep operator learning frame that utilizes a small microstructural dataset to identify the nonlinear mechanical behavior of disordered metamaterials. Additionally, Park et al. [2] employed a dynamic approach to decouple the geometric effects on stiffness and vibrational features in 3D chiral structures through generative modeling. Furthermore, in [3], ultra-elastic constitutive formulations were developed, incorporating incremental 3D finite element (FE) modeling to derive mean stress-strain trajectories.Several studies [4,5] have focused on assessing collapse loads under a uniform average stress to identify the stress threshold. In this context, 1D structural elements serve as an alternative approach to manage complex 3D hexahedral grids, utilizing the lower bound theorem to estimate the collapse limit directly. Although repeatedly algorithms have been proposed in the literature to couple finite element (FE) analysis with limit analysis [6,7], the method discussed here offers greater computational productivity and a more direct way to estimate the ultimate limit load. Researchers have expanded the literature beyond linear elasticity by examining post-yield behavior and plastic responses, especially in systems where high energy dissipation, cyclic load resilience, and long-term durability are critical. For instance, Song et al. [10] investigated the effects of geometric hierarchy on the localization of plastic strain and the complement of energy absorption in compressively loaded hierarchical structures. Experimental methodologies, especially when combined with fracture morphology analysis and high-fidelity strain field mapping, are essential for validating numerical modeling and evaluating such complex phenomena. Moreover, plasticity plays a crucial role in origami- and kirigami-inspired metamaterials, where localized folding zones represent important failure modes or are intentionally designed as deformable areas. The mechanical behavior of a deformable origami-based structure was analyzed under cyclic and high-strain loads, yielding encouraging results for the development of bioengineering scaffolds [13]. Additionally, Li et al. [14] investigated nonlinear elastic and plastic behavior in architected structures by combining physical and mechanical tests with resemblant numerical modelings and in situ observational data. Researchers have recently examined the assimilation of mechanical modeling with programmable or active components that can control or trigger plastic deformation as a functional mechanism. A study reported in [15] proposed an embedded actuator-driven reconfigurable mechanical system. Meanwhile, [16] provided a comprehensive review of the design principles underlying active structures. Key characteristics of such systems include dynamic stiffness flexibility and controlled shifts between varied deformation modes. This paper focuses on a systematic evaluation of both elastic and plastic performance to understand the micro-scale mechanical behavior of structured metamaterials. The primary goal is to propose an effective numerical methodology to assess the ultimate strength of these materials, referred

to as periodic micro-structured continua. These materials demonstrate periodic repetitions and perform as essential building blocks for complex frameworks, suggesting significant potential for developing performance-oriented structures through additive manufacturing (AM) [3,19–22]. The octet-truss lattice is analyzed within the elastic range using ANSYS to investigate its mechanical behavior under virtual loading. The resulting stiffness matrix is then utilized to assess material isotropy based on Zener's criterion, allowing for the identification of specific density configurations that demonstrate isotropy. To extend the analysis into the plastic regime, a pioneering finite element limit analysis technique developed by the authors (FELA) [4] is employed. This method is based on the lower bound theorem [23–26] and utilizes self-equilibrated stress fields characterized by discrete nodal parameters to define admissible stress states. The objective is to identify the maximum load that is in equilibrium with these admissible fields, representing the ultimate collapse threshold. The paper depicts the potential role of AI in the homogenization process within both the elastic and plastic ranges. By merging AI into the FELA procedure, it becomes possible to create clusters and sub-clusters for lattice representative volume elements (RVEs) that describe the composition of metamaterials.

2 Computational Characterization of RVEs: Homogenization and Limit Analysis

The elastic homogenization and the evaluation of isotropic characteristics are performed within specific, well-established configurations of structured metamaterial Representative Volume Elements (RVEs). In particular, the study examines a cubic topology: a truss-based architecture merging Body-Centered Cubic (BCC) and Pure Cubic (PC) geometries, which termed the isotropic truss; an equivalent star-system, and an octet truss, as represented in Figure 1.

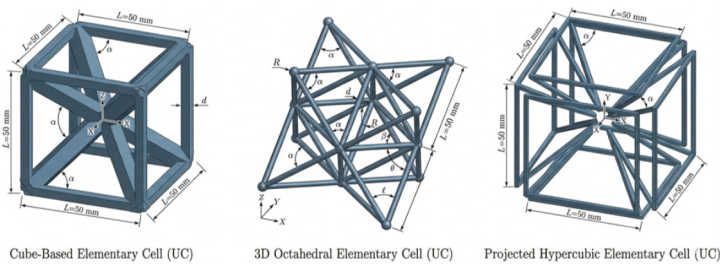

Fig. 1. case study representation

The objective of the research focuses on implementing the AI in a well-established limit analysis framework for these unit cells, aimed at improving the calculation performance on massive lattice RVEs. This section outlines a succinct overview of the methodology employed to assess the elastic properties of

the metamaterial architectures. The adopted approach is informed by the theoretical foundations established by Lakes [27], who derived estimates for elastically isotropic lattices characterized by stretching-dominated mechanisms at the mesoscopic scale. It is also based on the report in [28] regarding the topology optimization of isotropic truss structures. Drawing on earlier works, analytical criteria of lattice topologies are formulated so that microscopic elastic isotropy is obtained.

2.1 Constitutive Modeling of the Equivalent Elastic Continuum

FE modeling is implemented to capture the elastic behavior of such structures, in which uniform macroscopic strain fields are applied to representative unit cells. This study also uses periodic boundary conditions (PBCs) to ensure mechanical compatibility throughout the RVE. Unit cells are simulated in the form of a beam element frame with axial and flexural degrees of freedom (DOFs) in the nodes. It should be noted that the consistency of the mechanical response does not change upon the replacement of the beams with link elements serving as totally axial rods. This study employs 1D elements that address not only pure flexural (bending) behavior but also pure axial (extensional) behavior for the simulation of representative unit cells. The mean fields of continuum mechanics are used to characterize the homogenized medium, including the displacement vector field $\mathbf{u}(\mathbf{x}) = \{u_1, u_2, u_3\}$, the derived strain tensor field $\boldsymbol{\varepsilon}$, and the resultant stress tensor field $\boldsymbol{\sigma}$.

$$\begin{aligned} \boldsymbol{\varepsilon} &= \frac{1}{2}\left(\nabla^T \mathbf{u} + \nabla \mathbf{u}\right) \\ \boldsymbol{\sigma} &= \mathbf{C}\boldsymbol{\varepsilon} \end{aligned} \tag{1}$$

Where $\mathbf{C}$ is the fourth-order elastic tensor of the homogenized continuum. Voigt notation is used to reformulate the second- and fourth-order tensors for subsequent FE analysis. Index contraction transforms the elastic tensor into a symmetrical 6×6 second-order matrix. A predefined elementary strain (specifically a unit strain from the strain basis) is imposed on the framed structure to obtain the RVE stress using simultaneous nodal displacements applied throughout all faces of the cube (see Fig. 1). Then, the resulting mean strain is:

$$\varepsilon_{ij} = \frac{1}{2}\left(\frac{u_i(x_j)}{\Delta x_j} + \frac{u_j(x_i)}{\Delta x_i}\right) \tag{2}$$

The nodal reaction forces are used to obtain the homogenized stress components:

$$\sigma_i = \frac{\sum_n F_i}{A_i} \tag{3}$$

where all nodes on face i of the cube with an area of A_i are incorporated into the summation. A unit strain vector is used for each fundamental case, with the corresponding columns of the elastic stiffness matrix comprising the resulting stress components. Translational DOFs constitute the predefined nodal displacements

to trigger a unit strain. This study neglects rotational DOFs due to their inconsistency with the standard 3D Cauchy continuum model. The anisotropy of the material is determined using the symmetry classification of the elasticity matrix **C**. Based on Lord Kelvin's theories, Cowin et al. [29–32] comprehensively classified anisotropy in the elastic tensor **C**. For the cubic RVE, the equivalent material's elastic tensor reduces to three independent constants. In Voigt notation [33], this cubic elastic matrix is expressed as:

$$\mathbf{C} = \begin{bmatrix} C_{11} & C_{12} & C_{13} & 0 & 0 & 0 \\ C_{12} & C_{22} & C_{23} & 0 & 0 & 0 \\ C_{13} & C_{23} & C_{33} & 0 & 0 & 0 \\ 0 & 0 & 0 & C_{44} & 0 & 0 \\ 0 & 0 & 0 & 0 & C_{55} & 0 \\ 0 & 0 & 0 & 0 & 0 & C_{66} \end{bmatrix} \tag{4}$$

This symmetry is characterized by the equalities $C_{11} = C_{22} = C_{33}$, $C_{12} = C_{13} = C_{23}$, and $C_{44} = C_{55} = C_{66}$.

In this study, a preliminary simplified analysis is performed to verify the isotropic properties of the homogenized medium. Isotropic materials are defined by a specific elastic matrix that depends on only two independent parameters: the Lamé constants, μ and λ:

$$\mathbb{C} = \begin{bmatrix} 2\mu+\lambda & \lambda & \lambda & 0 & 0 & 0 \\ \lambda & 2\mu+\lambda & \lambda & 0 & 0 & 0 \\ \lambda & \lambda & 2\mu+\lambda & 0 & 0 & 0 \\ & & & \mu & 0 & 0 \\ & Symm & & 0 & \mu & 0 \\ & & & 0 & 0 & \mu \end{bmatrix} \tag{5}$$

Given the structure of the isotropic matrix, the Zener ratio (z) is defined as:

$$z = \frac{C_{11} - C_{12}}{2C_{44}} \tag{6}$$

For isotropic materials, this ratio is unity, and any variance from this value serves as a numerical indicator of the material's anisotropy [34,35]. Computational analysis verifies that the stiffness matrix **C** comprises two 3×3 diagonal blocks, while the off-diagonal 3×3 blocks are zero. Furthermore, the lower-right submatrix simplifies to a strictly diagonal form.

As an example, the results obtained for an Isotropic truss configuration are reported below in the following Table 1.

Table 1. Parametric Analysis of the Isotropic Truss: Identifying the Unitary Zener Coefficient

d_{FCC} (mm)	d_{PC} (mm)	ρ	Zener Link Element	Zener Beam Element
0.10	0.40	4.00	6.07	6.04
0.15	0.40	2.67	2.74	2.72
0.22	0.40	1.82	1.29	1.27
0.23	0.40	1.74	1.19	1.16
0.24	0.40	1.67	1.08	1.07
0.25	**0.40**	**1.60**	**1.00**	**1.00**
0.30	0.40	1.34	0.71	0.69
0.40	0.40	1.00	0.42	0.39

2.2 Evaluation of Ultimate Strength via Limit Analysis

To determine the peak load-bearing capacity of the lattice RVE, a direct numerical strategy is employed based on the lower bound theorem [4]. This study calculates the collapse load multipliers and determines the macroscopic yield domain of the homogenized medium to incorporate constituent properties and structure using finite element limit analysis (FELA). The representative macrostresses, i.e., the nodal forces (Eq. (3)), are used in the lower bound technique to find the critical force magnitudes at collapse, and FELA considers the limit load to be the maximum sustainable threshold that meets the material yield and mechanical compatibility criteria.

This study reviews FELA concisely to elaborate on the fundamental principles. First, the manifold of admissible stress states is identified. Admissible stress fields in the structure are the superposition of the elastic response σ^e, which is obtained from the loads applied in an ideal elastic framework, and a self-equilibrating stress field σ_0^e. The multiplicity of balance equations governed by $E_{eq}(f)$ must be met by the self-equilibrated state:

$$\sigma \in E_{eq}(f) \iff \langle \sigma, \delta\epsilon \rangle = 0, \quad \forall \delta u, \delta\epsilon \tag{7}$$

RVE mechanical equilibrium is divided into a primary equation and an ideal elastic equation, with the former reflecting the real stress distribution and the latter incorporating the stress field induced inside a theoretical material under a linear elastic constitutive law.

$$\begin{cases} \langle \sigma, \delta\epsilon \rangle - \langle f, \delta u \rangle = 0 & \text{for the actual structure} \\ \langle \sigma^e, \delta\epsilon \rangle - \langle f, \delta u \rangle = 0 & \text{for the indefinitely elastic structure} \\ \langle \sigma^e + \sigma^{0e}, \delta\epsilon \rangle - \langle f, \delta u \rangle = 0 & \text{for the actual structure} \\ \langle \sigma^{0e}, \delta\epsilon \rangle = 0 \implies \sigma^{0e} \in \text{Null}(E_{eq}) & \text{Null space definition} \end{cases} \quad \forall \delta u, \delta\epsilon \tag{8}$$

An admissible stress state is a state remaining in the elastic domain (D^e) boundaries, which ensures that no increment occurs in the plastic strain rate ϵ^p:

$$\dot{\epsilon}^p = 0 \iff \sigma \in \text{int}(D^e) \tag{9}$$

Here, σ^{0e} is a crucial parameter, and the self-equilibrated stress manifold is to be analyzed comprehensively through a vector basis for the Null(E_{eq}) space, which is constructed in FELA based on nodal parameters and the shape functions used in the description of FE displacement fields.

Despite procedural versatility in several types of elements, Bernoulli beam elements are employed in the proposed RVE model. In this context, the local self-equilibrated stresses reduce to ordinary element forces, such as axial forces N, shear forces S_i, and bending moments M_i with $i \in \{1, 2\}$, defined along the axes of the element's cross-sectional plane. Although shear effects are often neglected in specific applications, the effective stress and generalized strain vectors are generally established as:

$$\begin{aligned} \sigma &= \{N, M_1, M_2\} \\ \epsilon &= \{\Delta u_3, \chi_1, \chi_2\} \end{aligned} \tag{10}$$

By analyzing the structural response under zero external loading, the self-equilibrating stress field can be defined as a linear mapping of the vector δ. This vector comprises nodal parameters that represent the permanent strains at the element level alongside the displacements of constrained nodes. As detailed in the direct formulation presented in [4], a linear operator V is established to link these parameters to the generalized self-equilibrated stress components:

$$\sigma^{0e} = V\delta \tag{11}$$

where the generalized stress vector is composed of:

$$\sigma^{0e} = \{N^{0e}, M_1^{0e}, M_2^{0e}\} \tag{12}$$

The elastic domain for each RVE, which encapsulates the compatibility requirements, is characterized as an ellipsoidal volume within a three-dimensional framework, with its primary axes defined by the following boundary constraints:

$$\begin{aligned} N_y^- < N < N_y^+ \\ M_{1y}^- < M_1 < M_{1y}^+ \\ M_{2y}^- < M_2 < M_{2y}^+ \end{aligned} \tag{13}$$

In this formulation, the indices iy^+ and iy^- denote the positive and negative yield thresholds for the generalized stress components within the element's cross-sectional plane.

To determine these limits, the RVE is subjected to natural boundary conditions, where nodal forces are applied to a specific cubic face; these forces act normal to the surface for axial limits and parallel to it for shear limits. Furthermore, essential boundary conditions are implemented via periodic displacement

constraints, ensuring a consistent and repetitive stress field across the continuum. Based on this beam-element RVE model, the derived elastic stress vector is defined as follows:

$$\sigma^e = \{N^e, M_1^e, M_2^e\} \tag{14}$$

By scaling the applied loads with a scalar factor k, the collapse load multiplier s_c is determined through the following optimization program:

$$s_c = \max_{k,\sigma^{0e} \in \mathrm{Null}(E_{eq})} k \quad \text{subject to:} \quad \begin{pmatrix} N_y^- < kN^e + N^{0e} < N_y^+ \\ M_{1y}^- < kM_1^e + M_1^{0e} < M_{1y}^+ \\ M_{2y}^- < kM_2^e + M_2^{0e} < M_{2y}^+ \end{pmatrix} \tag{15}$$

The peak force derived from the program identifies the yield stress, representing the intersection of the homogenized material's elastic domain with the stress axes.

This approach bypasses iterative, path-dependent methods, directly identifying the stress limit as the supremum of the lower bound. By applying this procedure to various lattice geometries, the collapse multipliers are determined, defining the axes of a six-dimensional hyper-ellipsoidal limit locus. It is important to clarify that this domain is defined within a special stress space based on the RVE's cubic faces, distinct from the Haigh–Westergaard representation. The normal-to-shear stress limit ratio was estimated by the von Mises criterion to be $\sqrt{3}$, whereas such a σ_0/τ_0 ratio was numerically found to be violated repeatedly, depending on PC and BCC proportions. This suggests that no plastic isotropy existed.

3 Method

3.1 Automated RVE Generation Framework

The proposed method incorporates AI for automatic Representative Volume Element (RVE) generation, significantly decreasing the reliance on manual CAD modeling.

A schematic representation or input image is used to identify zones containing material through a learning-based technique. This process trains the AI algorithm to recognize structural designs and distinguish between solid regions and voids. However, the AI cannot assess the feasibility of constructing the generated structures. Therefore, AI-driven generation is integrated with computational procedures through a comprehensive multi-stage pipeline (see Fig. 4).

In Stage 1, deep learning techniques, specifically vision alters and convolutional neural networks (CNNs), are employed to segment input images into 2D masks. These masks are then extruded to create raw 3D geometries.

The AI component approaches the identification of structural features as a dense, pixel-wise classification problem. For semantic segmentation, the algorithm assigns a discrete class label $c \in \{1, \ldots, K\}$ to every pixel x_i (representing

material or void), where the network outputs a continuous tensor of logits $z_{i,c}$. These logits are converted into a probability distribution using the Softmax function:

$$P(y_i = c|X) = \frac{\exp(z_{i,c})}{\sum_{k=1}^{K} \exp(z_{i,k})} \tag{16}$$

where X is the input image and y_i is the predicted class for pixel i. The final predicted class $\hat{y}_i$ is the one that maximizes this probability: $\hat{y}_i = \arg\max_c P(y_i = c|X)$. This ensures a precise transition from raw pixel intensities to discrete physical components like load-bearing struts.

To refine the model's accuracy during the training phase, a categorical Cross-Entropy ($\mathcal{L}_{CE}$) loss function is minimized over all N pixels:

$$\mathcal{L}_{CE} = -\frac{1}{N} \sum_{i=1}^{N} \sum_{c=1}^{K} y_{i,c} \log(P(y_i = c|X)) \tag{17}$$

where $y_{i,c}$ is the binary indicator (0 or 1) if class label c is the correct classification for pixel i. This rigorous mathematical optimization allows the pipeline to maintain high geometric fidelity, which is essential for the subsequent multiscale mechanical analysis.

Due to the inherently stochastic nature of AI generation, an essential structural admissibility filter is applied in Stage 2 to eliminate configurations that exhibit geometric inconsistencies or mechanical instability. Stage 3 involves parameterizing the admissible geometries into either discrete node-and-strut networks or continuous implicit surfaces. Finally, in Stage 4, finite element analysis (FEA) is conducted on the multiscale models to derive homogenized elastic properties, calculate collapse multipliers, and determine the macroscopic yield domain using finite element limit analysis (FELA).

Due to the stochastic nature of AI-generated outputs, a filtering stage is required. Generated RVEs may include:

- geometrically inconsistent structures,
- mechanically unstable (labile) configurations,
- disconnected or non-manufacturable geometries.

A selection process is implemented to retain only structurally admissible Representative Volume Elements (RVEs). This step guarantees that the modeling and analysis phases are conducted on configurations that are physically meaningful.

Discrete RVEs are represented as networks of nodes and struts, with each node defined by its spatial coordinates.

$$\mathbf{P}_i = (x_i, y_i, z_i) \tag{18}$$

Nodes are approximated as spheres (or polyhedral approximations such as icosahedra), defined by:

$$(x - x_i)^2 + (y - y_i)^2 + (z - z_i)^2 \leq R_{\text{joint}}^2 \tag{19}$$

Struts connecting nodes P_1 and P_2 are modeled as cylindrical elements whose axis is defined parametrically:

$$\mathbf{L}(t) = \mathbf{P}_1 + t(\mathbf{P}_2 - \mathbf{P}_1), \quad 0 \leq t \leq 1 \tag{20}$$

The strut surface is obtained by enforcing a constant radial distance from the axis, see Fig. 2.

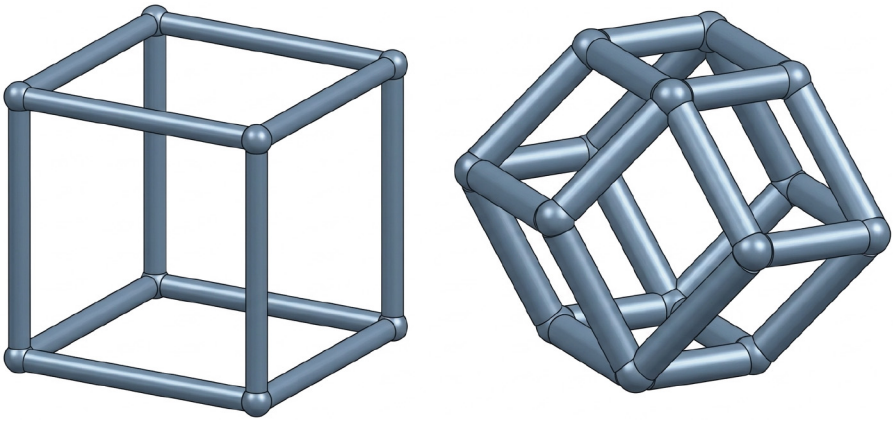

Fig. 2. Example of strut-based lattice geometry

3.2 Implicit Geometry: Surface-Based Metamaterials

Implicit geometries are defined through continuous scalar fields over a discretized 3D domain. The spatial coordinates are scaled as:

$$X = \omega x, \quad Y = \omega y, \quad Z = \omega z \tag{21}$$

A scalar field $F(X, Y, Z)$ is evaluated, and the geometry is extracted as an iso-surface:

$$F(X, Y, Z) = c \tag{22}$$

The discretization uses the Marching Cubes algorithm to reconstruct complex geometries, such as Triply Periodic Minimal Surfaces (TPMS).

Image segmentation is used to convert pixel-based information into structural geometry. The image domain is partitioned into regions R_i satisfying:

- completeness,
- exclusivity,
- homogeneity,
- separability.

Deep learning models, such as CNNs or Vision Transformers, are used to assign class labels to each pixel. The Softmax function computes the probability distribution over these classes:

$$P(y_i|X) \tag{23}$$

The final classification utilizes maximum likelihood prediction. Individual structural components are differentiated through instance segmentation. The Intersection over Union (IoU) metric is employed to assess the quality of segmentation:

$$IoU(A, B) = \frac{|A \cap B|}{|A \cup B|} \tag{24}$$

Geometric fidelity is represented by high IoU-values.

4 Results

4.1 Image-to-Geometry Conversion

Input images are effectively transformed into 3D geometries by the trained AI algorithm, with discretization algorithms being used for the extrusion and processing of segmentation masks into solid models.

The standard formats for the exportation of the obtained geometries include (Fig. 3):

- `.dwg` (CAD),
- `.obj` (mesh-based),
- `.stl` (additive manufacturing),
- `.stp` (FEM).

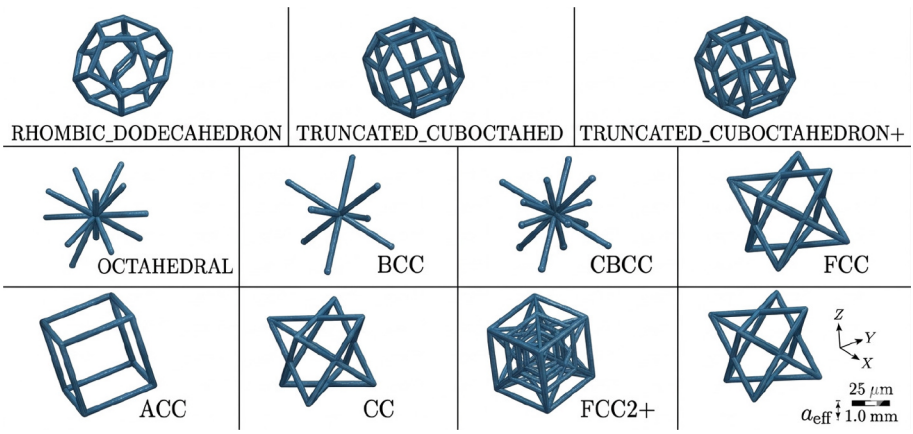

Fig. 3. Example of strut-based lattice geometry

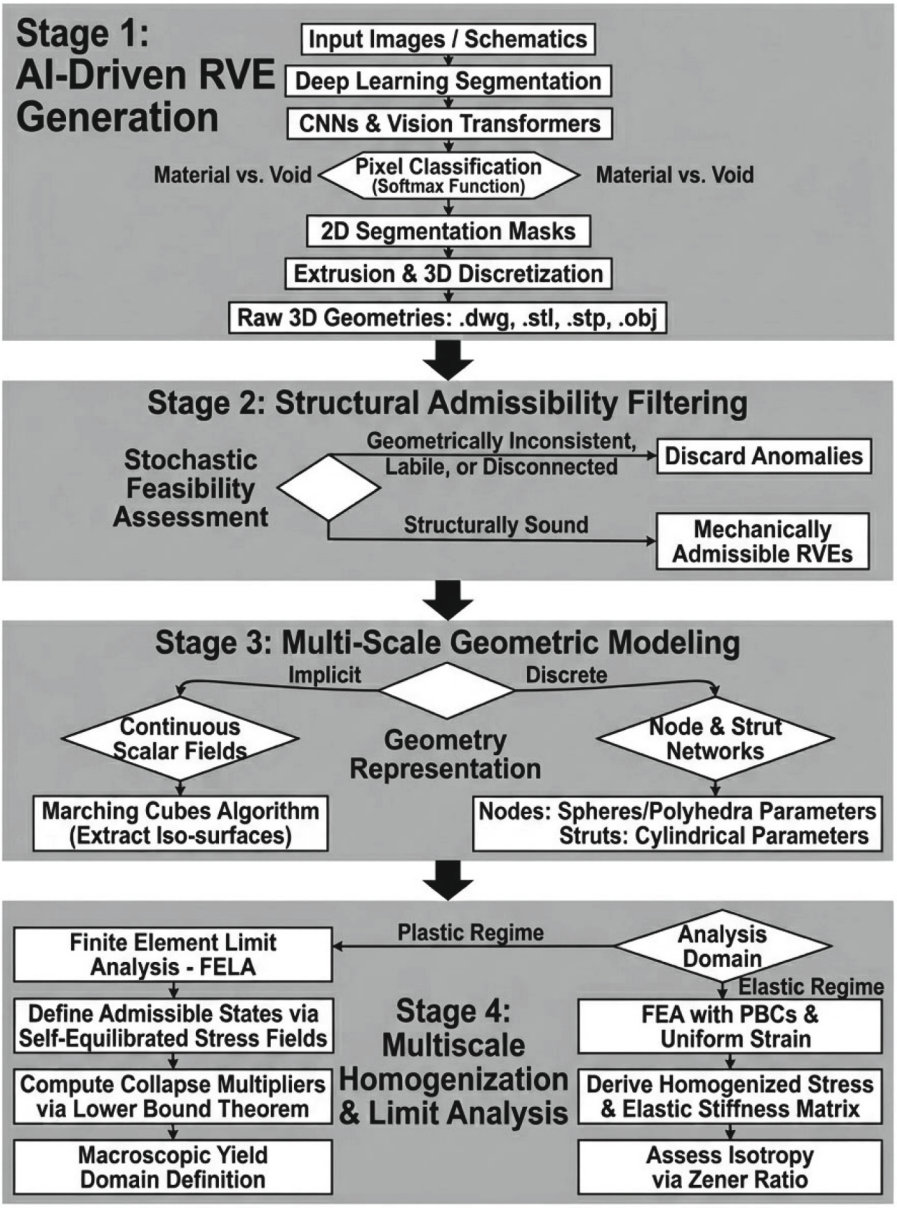

Fig. 4. Diagram of automated generation, structural filtering, geometric modeling, and multiscale mechanical assessment of metamaterial RVEs

4.2 Generated RVEs

The pipeline produced a number of RVEs. Drawing on this procedure, highly complex geometries with marginal manual intervention can be generated.

Preprocessing is remarkably accelerated by directly using such geometries in FE analysis.

This study evaluated a cantilever beam comprising isotropic truss RVEs.

$$\kappa = \frac{h}{\delta} \tag{25}$$

The effect of the geometric parameter on mechanical performance was analyzed, with h and δ denoting the characteristic cell size and strut thickness, respectively.

5 Conclusions

This study combines artificial intelligence (AI) and computational mechanics to develop a method for the automatic generation, filtering, and analysis of Representative Volume Elements (RVEs) for mechanical metamaterials. The integrated approach converts image-based inputs directly into 3D geometries suitable for finite element (FE) analysis and machine learning (ML). By using automated renovator algorithms alongside learning-based segmentation, this method quite reduces the demand for manual CAD modeling, thereby speeding up the preprocessing stage.

Filtering is a vital part of this approach, as it makes certain that the architectures generated by AI are mechanically valid. This is essential for applying data-driven generation techniques to real-world engineering problems. Homogenization was applied to evaluate the mechanical performance of representative volume elements (RVEs) in both elastic and limit states. It was shown that geometric parameters, particularly the ratio of cell size to strut thickness, are highly dependent on key properties. The modulus of elasticity obtained was significantly lower than that of the base material, and the numerical results were in good assent with experimental data obtained in [37–39] (error $\approx 7\%$).

Additionally, the represented method demonstrated a notable calculable improvement; the computational cost was 95% lower than standard modeling techniques, as fewer elements were used for complex lattice designs. The computational cost for highly intricate unit cells was even lower.

Several limitations were encountered in the study. First, only a single material and a limited number of lattice design classes were analyzed. Second, the AI algorithm did not guarantee the feasibility of the structures, indicating the need for external validation and filtering processes.

It is recommended that researchers expand the proposed approach to include multimaterial systems to improve the robustness of AI-based generation. Additionally, incorporating physics-informed constraints into the learning process could be beneficial. Exploring more complex loadings and real-scale structural applications is also suggested.

Overall, the proposed method considerably contributes to the automation of metamaterial design, which enables the development of efficient, scalable, and data-driven methods for advanced structural engineering.

References

1. Cao, Q., Li, Y., Wang, Y., Zhang, J., Gu, G.X.: Characterization and inverse design of stochastic mechanical metamaterials. Adv. Mater. **37**, 240063 (2025). https://doi.org/10.1002/adma.202420063
2. Park, J., Noh, J., Shin, J., Gu, G.X., Rho, J.: Investigating static and dynamic behaviors in 3D chiral mechanical metamaterials by disentangled generative models. Adv. Funct. Mater. **34**, 2412901 (2024). https://doi.org/10.1002/adfm.202412901
3. Chen, Z., Mordehai, D.: Homogenization of the yield surface of body-centered cubic and octet lattice structures under multiaxial loadings. Int. J. Solid Struct. **320**, 113486 (2025). https://doi.org/10.1016/j.ijsolstr.2025.113486
4. Zona, R., Ferla, P., Minutolo, V.: Limit analysis of conical and parabolic domes based on semi-analytical solution. J. Build. Eng. **44**, 103271 (2021). https://doi.org/10.1016/j.jobe.2021.103271
5. Zona, R., Esposito, L., Palladino, S., Minutolo, V.: Dislocation-Based Finite Element Method for Homogenized Limit Domain Characterization of Structured Metamaterials; Engineering Computations: Swansea, UK (2024). https://doi.org/10.1108/EC-12-2023-0970
6. Casciaro, R., Garcea, G.: An iterative method for shakedown analysis. Comput. Methods Appl. Mech. Eng. **191**, 5761–5792 (2002). https://doi.org/10.1016/S0045-7825(02)00496-6
7. Garcea, G., Armentano, G., Petrolo, S., Casciaro, R.: Finite element shakedown analysis of two-dimensional structures. Int. J. Numer. Methods Eng. **63**, 1174–1202 (2005). https://doi.org/10.1002/nme.1316
8. Fong, E., Koponen, K., Omairey, S., Dunning, P.: Developing mechanical metamaterials under an adaptable topology optimization design framework. Front. Mech. Eng. **18**, 379 (2023). https://doi.org/10.1007/s10338-023-00379-y
9. Fong, E., Koponen, K., Omairey, S., Dunning, P.: Thermal-mechanical metamaterial analysis and optimization using finite element software. Eng. Comput. **39**, 1855–1872 (2023). https://doi.org/10.1007/s00366-023-01855-2
10. Song, J., Yan, J., Yi, B.: Design, fabrication, and characterization of hierarchical mechanical metamaterials. Front. Mech. Eng. **19**, 3 (2024). https://doi.org/10.1007/s11465-023-0776-9
11. Kayacan, M.Y., Yılmaz, M.S., Üzün, A.: Mechanical characterization of metamaterials manufactured by a novel hybrid SLM technique utilizing powder metallurgy. Met. Mater. Int. **30**, 280 (2024). https://doi.org/10.1007/s12540-024-01846-y
12. Álvarez-Trejo, A., Cuan-Urquizo, E., Bhate, D., Roman-Flores, A.: Mechanical metamaterials with topologies based on curved elements. Mater. Des. **233**, 112190 (2023). https://doi.org/10.1016/j.matdes.2023.112190
13. Bagheri, M.A., Aubin, C.É., Nault, M.-L., Villemure, I.: Mechanical characterization of an origami-inspired super deformable metamaterial. Mater. Des. **233**, 113701 (2025). https://doi.org/10.1016/j.matdes.2025.113701
14. Uddin, K.Z., Heras, M., Youssef, G., Kiel, T., Koohbor, B.: Multiscale experimental characterization of nonlinear mechanics and auxeticity in mechanical metamaterials with rotating squares. Compos. Struct. **357**, 118931 (2025). https://doi.org/10.1016/j.compstruct.2025.118931
15. Zhang, Y., Wang, X., Liu, H., Li, Z., Wang, Y.: Reprogrammable mechanical metamaterials via passive and active magnetic interactions. Adv. Mater. **37**, 2412353 (2025). https://doi.org/10.1002/adma.202412353

16. Lu, M., Feng, L., Chen, Y.: Recent progress in active mechanical metamaterials. Adv. Sci. **8**, 2102662 (2021). https://doi.org/10.1002/advs.202102662
17. Kazim, M., Pal, A., Goswami, D.: Mechanical metamaterials for bioengineering. Adv. Eng. Mater. **27**, 2401806 (2025). https://doi.org/10.1002/adem.202401806
18. Zhang, Y., Wang, X., Liu, H., Li, Z., Wang, Y.: Mechanical metamaterials for sensor and actuator applications. Int. J. Precis. Eng. Manuf. **24**, 549–561 (2023). https://doi.org/10.1007/s40684-023-00549-w
19. DeLuca, A., Greco, A., Perfetto, D., Sepe, R.: Influence of building position and printing scheme on mechanical properties of fused filament fabrication PLA specimens. In: Macromolecular Symposia, vol. 411 (2023). https://doi.org/10.1002/masy.202300024
20. Greco, A., De Luca, A., Sepe, R., Gerbino, S.: Investigation on tensile properties of FFF PEEK: effects of printing parameters and post-processing treatment. Procedia Struct. Integr. **53**, 178–184 (2024). https://doi.org/10.1016/j.prostr.2024.01.022
21. Iandiorio, C., Serenella, R., Salvini, P.: A combined approach of experimental testing and inverse FE modelling for determining homogenized elastic properties of membranes and plates. Eng. Proc. **85**, 27 (2025). https://doi.org/10.3390/engproc2025085027
22. Mandolesi, B., Iandiorio, C., Belardi, V.G., Vivio, F.: Spinodal decomposition-inspired metamaterial: tailored homogenized elastic properties via the dimensionless Cahn-Hilliard equation. Eur. J. Mech. A. Solids **112**, 105615 (2025). https://doi.org/10.1016/j.euromechsol.2025.105615
23. Bleich, H.: Über die Bemessung statisch unbestimmter Stahltragwerke Berücksichtigung des elastisch-plastischen Verhaltens. Bauingenieur **19**, 261–266 (1932)
24. Melan, E.D.: Spannungszustand eines Mises-Henckyschen Kontinuums bei veraender licker Belastung. Sitzber. Akad. Wiss. **147**, 73–78 (1938)
25. Melan, E.: Zur Plastizität des rälicken Kontinuums. Ing. Arch. **8**, 116–126 (1938). https://doi.org/10.1007/BF02084409
26. Zona, R., Minutolo, V.: A dislocation-based finite element method for plastic collapse assessment in solid mechanics. Arch. Appl. Mech. **94**, 6 (2024). https://doi.org/10.1007/s00419-024-02594-6
27. Lakes, R.S.: Negative-Poisson's-ratio materials: auxetic solids. Annu. Rev. Mater. Res. **47**, 63–81 (2017). https://doi.org/10.1146/annurev-matsci-070616-124118
28. Julie, J.A., et al.: Field responsive mechanical metamaterials. Sci. Adv. **4**, eaau6419 (2018). https://doi.org/10.1126/sciadv.aau6419
29. Thomson, W.K. (Lord Kelvin), Elasticity. In: Encyclopaedia Britannica. Edinburgh (1878)
30. Cowin, S.C., Mehrabadi, M.M., Sadegh, A.M.: Kelvin formulation of the anisotropic Hooke's law. In: Modern Theory of Anisotropic Elasticity. SIAM (1991)
31. Cowin, S.C., Mehrabadi, M.M.: On the structure of the linear anisotropic elastic symmetries. J. Mech. Phys. Solids **40**, 1459–1472 (1992). https://doi.org/10.1016/0022-5096(92)90029-2
32. Cowin, S.C., Mehrabadi, M.M.: Anisotropic symmetries of linear elasticity. Appl. Mech. Rev. **48**, 247–285 (1995). https://doi.org/10.1115/1.3005102
33. Gurtin, M.E.: The linear theory of elasticity. In: Encyclopedia der Physics. Springer (1972). https://doi.org/10.1007/978-3-662-39776-3_1
34. Gazis, D.C., Tadjbakhsh, I., Toupin, R.A.: The elastic tensor of given symmetry nearest to an anisotropic elastic tensor. Acta Cryst. **16**, 917–922 (1963). https://doi.org/10.1107/S0365110X63002449
35. Norris, A.N.: The isotropic material closest to a given anisotropic material. J. Mech. Mater. Struc. **1**, 223–238 (2006). https://doi.org/10.2140/jomms.2006.1.223

36. Minutolo, V., Zona, R.: Numerical evaluation of the homogenized limit domain of structured metamaterials. In: Proceedings of HICOMP, Rhodes (2025). https://hicomp2025.org/proceedings/pdf/24416.pdf
37. Greco, A., Russo, M.B., Cardilicchio, A., Gerbino, S.: The simultaneous effect of FFF build orientation on tensile strength, flatness and roughness. In: Proceedings of ADM 2023. Springer, Cham (2025). https://doi.org/10.1007/978-3-031-76597-1_1
38. Greco, A., De Luca, A., Gerbino, S., Lamanna, G., Sepe, R.: Influence of infill pattern and layer height on surface characteristics and fatigue behavior of FFF-printed PEEK. Fatigue Fract. Eng. Mater. Struct. **47**(12), 4741–4754 (2024). https://doi.org/10.1111/ffe.14450
39. Greco, A., De Luca, A., Sepe, R., Gerbino, S.: Investigation on tensile properties of FFF PEEK: effects of printing parameters and post-processing treatment. Procedia Struct. Integr. **53**, 178–184 (2024). https://doi.org/10.1016/j.prostr.2024.01.022